Mapping the magnetic and crystal structure in cobalt nanowires

Jesus Cantu-Valle,[1] Israel Betancourt,[1,a)] John E. Sanchez,[1] Francisco Ruiz-Zepeda,[1] Mazin M. Maqableh,[2] Fernando Mendoza-Santoyo,[1,b)] Bethanie J. H. Stadler,[2] and Arturo Ponce[1,c)]

[1]*Department of Physics and Astronomy, University of Texas at San Antonio, One UTSA Circle, San Antonio, Texas 78249, USA*

[2]*Electrical and Computer Engineering, University of Minnesota, 4-174 EE/CSci Bldg., 200 Union St. SE, Minneapolis, Minnesota 55455, USA*

(Received 3 April 2015; accepted 23 June 2015; published online 8 July 2015)

Using off-axis electron holography under Lorentz microscopy conditions to experimentally determine the magnetization distribution in individual cobalt (Co) nanowires, and scanning precession-electron diffraction to obtain their crystalline orientation phase map, allowed us to directly visualize with high accuracy the effect of crystallographic texture on the magnetization of nanowires. The influence of grain boundaries and disorientations on the magnetic structure is correlated on the basis of micromagnetic analysis in order to establish the detailed relationship between magnetic and crystalline structure. This approach demonstrates the applicability of the method employed and provides further understanding on the effect of crystalline structure on magnetic properties at the nanometric scale. © *2015 AIP Publishing LLC*. [http://dx.doi.org/10.1063/1.4923745]

INTRODUCTION

For society to continue current technology trends, a comprehensive understanding of nanoscale materials and their physical properties are necessary within the scientific community. In particular, magnetic nanostructures of different size, shape, and composition (e.g., nanoparticles, nanowires, and thin films) possess a great potential to improve areas such as magnetic data storage and electromagnetic sensing.[1–4] Lately, magnetic nanowires (Co, Fe, and Ni) have been studied experimentally and by simulations.[5–8] For example, depending on their diameters, the magnetization of these nanowires is known to reverse via either transverse walls or vortex walls. In thin ferromagnetic nanowires (diameter < 40 nm), a simple domain wall nucleates and propagates along the nanowire axis, while the reversal of thick nanowires (diameter more than 40 nm) is achieved via localized curling or vortex mode.[7] The magnetization direction of each magnetic domain can also be influenced by the magnetocrystalline anisotropy, typically following the easy magnetization axis to minimize the magnetocrystalline energy. Therefore, the magnetization behavior in these nanostructures is dominated by the competition between shape anisotropy and magnetocrystalline anisotropy. In many cases, this competition can frustrate the magnetization. It is expected that the magnetostatic coupling between nanostructures will strongly influence their response to an external field, and therefore also influence subsequent device performance.[8–10]

However, it is difficult to observe the magnetization of individual nanowires and even more difficult to observe the crystalline grains within a nanowire. Some bulk measurements, such as first order reversal curves (FORC), can be used to observe averages and distributions of magnetizations and coercivities.[11] Magnetic force microscopy can image magnetization along a nanowire.[12,13] Other techniques use scattering to observed periodicities in magnetization and/or structure, for example, small angle neutron scattering (SANS).[14] Magnetic imaging in transmission electron microscopy (TEM) can be performed in different modes such as differential phase contrast microscopy, off-axis electron holography and Lorentz microscopy.[15–21] But the correlation between magnetization and individual grains has been elusive until recently.[22–27] In this matter, TEM offers the possibility to combine specialized techniques to investigate structure-property relationships at scales ranging from a few microns to a few nanometers.[28–33] For instance, off-axis electron holography affords the study of the magnetization distribution inside nanostructures in a detailed manner, while the coupling of nano-probe scanning and precession electron diffraction is a powerful technique developed to automatically obtain crystallographic orientation/phase maps of nanosized polycrystalline structures.[34] Precession electron diffraction (PED) is a technique that collects electron diffraction patterns under a conical oscillation of the electron beam leading in a significant reduction of the dynamical effects due to the thickness of the sample. In addition, PED provides oriented electron diffraction patterns even if the crystal is not perfectly aligned to a particular zone axis, which improves the measurements in the indexation process.[35]

In this work, the magnetization and crystalline orientations of high aspect ratio Co nanowires were mapped in a transmission electron microscope. The field of view of electron holography and PED-assisted automated crystal orientation mapping (ACOM) in TEM can vary from few

[a)]On Sabbatical leave from Instituto de Investigaciones en Materiales, Universidad Nacional Autónoma de México, C.P., D.F 04510 México, Mexico.

[b)]On Sabbatical leave from Centro de Investigaciones en Optica, A.C., León, Guanajuato, México, Mexico.

[c)]Author to whom correspondence should be addressed. Electronic mail: arturo.ponce@utsa.edu. Tel.: 210-458-8267.

nanometers to up to 2 μm.[36,37] The nanowires had diameters of 95 nm ± 5 nm and lengths of 240 nm–5.75 μm for aspect ratios (R = *Length/diameter*) that varied from 2.5 to 60. The magnetic flux distributions were experimentally observed using off-axis electron holography under zero magnetic field conditions, and phase maps were acquired and employed to distinguish magnetization from individual nanocrystals with high accuracy. The crystal structure was determined by TEM and mapped by ACOM-TEM. Finally, micromagnetic analysis was performed at individual nanowires to visualize and understand the effects of the crystallographic texture on the magnetization of the nanowire.

RESULTS

In order to perform a reliable magnetic analysis, we selected an isolated Co nanowire that was mounted on the carbon film of a lacey carbon copper grid. A TEM micrograph is presented in Figure 1(a), showing that no other nanowire is near the nanowire under study, thus avoiding any interaction of magnetostatic nature. An electron hologram of the nanowire was recorded as reference of the initial state of the Co nanowire, Figure 1(b), and its corresponding unwrapped phase image is displayed in Figure 1(c). Similar features were observed for another nanowire's holograms, as shown in supplementary Figure S1.[44]

In electron holography, phase information from several contributions regarding thickness, magnetic, electric, and stress fields can be resolved by means of suitable mathematical analysis.[38] In particular, the separation of electrostatic and magnetic phase shifts was performed by *in situ* magnetization reversal, carried out by the sequential application of magnetic fields of ±3.7 kOe, via the objective lenses, along the main axis of the nanowire, and computing the digital operation between the corresponding holograms (B+ and B−). The magnetic field applied was previously calibrated and the characterization of the contribution of the objective lens is included in supplementary Figures S2 and S3. The mathematical procedure on the images to extract separately the electrostatic or the magnetic contribution is described by the following equations:[26]

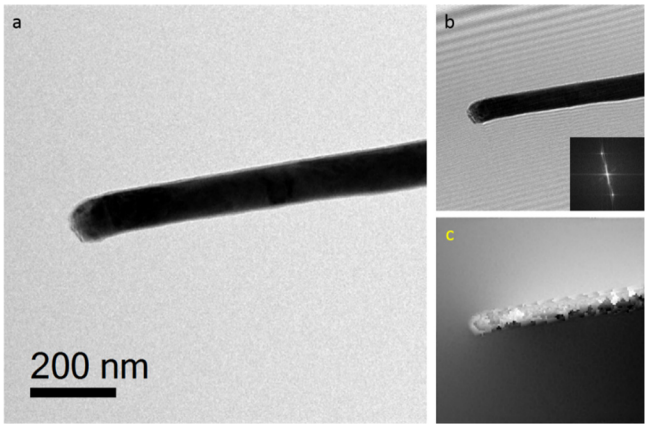

FIG. 1. (a) Low magnification TEM image of a Co nanowire. (b) Electron hologram where the inset shows the FFT from the sideband that was used to reconstruct the phase image. (c) Unwrapped phase image, displaying the phase variations characteristic of magnetic samples.

$$\frac{1}{2}[\varphi_2 + \varphi_1] = C_E V_o t, \tag{1}$$

$$\frac{1}{2}[\varphi_2 - \varphi_1] = \frac{e}{\hbar}\int\int B_\perp(x,y)\cdot dx \cdot dz, \tag{2}$$

where ϕ_1 and ϕ_2 correspond to the unwrapped phases extracted from B+ and B− holograms, respectively, C_E is an energy dependence constant, V_o is the mean inner potential of the material, t is the thickness of the nanowire, e is the electron's charge, h is the Planck constant, and $B_\perp$ correspond to the magnetic induction component normal to the plane containing the nanowire. The retrieved phases used for this analysis are shown in supplementary Figure S5. In this way, the electrostatic contribution obtained by Eq. (1) is shown in Figure 2(a), alongside its amplification (Figure 2(b)) obtained from three times the cosine of the electric phase. On the other hand, the pure magnetic phase contribution (Figure 2(c)) is obtained by computing half of the difference between supplementary Figures S5c and S5e, as stated in Eq. (2). The corresponding phase contour (displayed in Figure 2(d)) was amplified as three times the cosine of the magnetic phase image. These contours have a direct correspondence to the magnetic flux lines inside the nanowire, indicating a predominant axial orientation for the magnetization, including some marked deviations visualized as wavy flux lines. No magnetic domain wall was observed in this wire. In addition, the stray fields leaking around to the tip are a consequence of the formation of a vortex structure observed at the tip in which surrounding uncompensated flux lines results in the asymmetric magnetic contours observed in the image. The magnetic phase profile across the highlighted arrow in Figure 2(c) is plotted in Figure 2(e), showing that it corresponds to the predicted phase shift, consistent with the local magnetic induction within the nanowire.

A quantitative evaluation of the magnetic flux can be obtained from the retrieved phase maps, considering that between two adjacent contour lines there is a magnetic flux of $h/e = 4.1 \times 10^{-15}$ Wb, so a phase difference of 2π corresponds to a magnetic flux quantum of h/e. Then, the total phase shift ($\Delta\varphi$) across the nanowire in the unwrapped phase image is proportional to the total flux, thus the magnetization can be evaluated by the following equation:[26]

$$M = \frac{\Delta\varphi \cdot \phi_0}{2\pi \cdot \mu_0 \cdot S}, \tag{3}$$

where S is the cross-section area of the nanowire, μ_0 is the magnetic permeability of the vacuum, and ϕ_0 is the magnetic flux quantum (h/e). The magnetization was quantitatively evaluated from the total phase shift as $M = 1.42 \times 10^6$ A/m which correspond very well to the saturation magnetization of Co (of 1.43×10^6 A/m (Ref. 38)). To obtain the magnetic flux direction, it is necessary to compute the gradients (in both directions x and y) of the pure magnetic phase image. Then, the magnetic phase shift across the nanowire is proportional to the magnetic flux enclosed by the interfering trajectories of the electron beam.

In order to correlate the magnetic flux with crystalline structure, we performed PED-assisted ACOM in the same

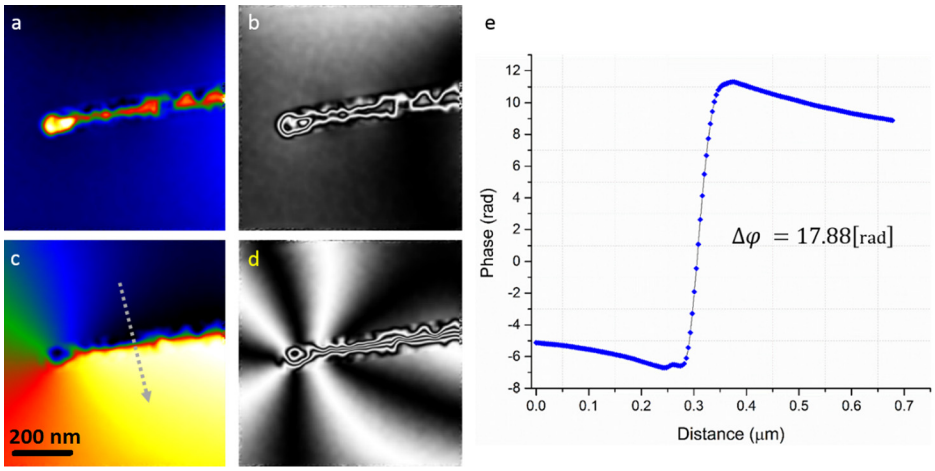

FIG. 2. (a) and (b) Electrostatic phase contribution and its corresponding amplification (three times the cosine of the electric phase), respectively. (c) and (d) Magnetic phase contribution and its corresponding amplification (three times the cosine of the magnetic phase), respectively. (e) Phase shift across the highlighted arrow in the magnetic phase image in (c).

nanowire. The PED-ACOM operation module is coupled with the microscope coils to scan the area of interest with a nanometer-sized electron beam (supplementary Figure S6), and record electron diffraction patterns at each step with an ultra-fast external charge coupled device camera (CCD). The spatial resolution of the crystal orientation map depends on the electron beam scanning step size and on the probe size used. The crystal structure of the nanowire was analyzed with the full set of diffraction patterns taken during the scanning session. The off-line data processing software performs spot recognition by template matching, computing the correlation index between the experimental spot pattern and the calculated spot pattern in the template. To estimate the degree of confidence of the pattern matching, a reliability map is generated from the two maximum values obtained from the correlation index. Its value ranges from zero-black to 100-white, and it indicates how safe or unique a solution is.[34] Additionally, an index map is generated which measures the degree of correlation, giving information on structural features according to the index matching. In this way, we obtain full information about the crystalline orientation and the degree of polycrystallinity in a fast and automated manner. For the Co nanowires, the best results yielded for the hexagonal phase, founding no cubic phase structure in the system. In Figure 3, the crystal orientation map of the same Co wire analyzed by electron holography is presented. In Figure 3(a), the crystal orientation map is displayed with respect to the "x" direction of the scanned area, and in Figure 3(b), the crystal orientation map is displayed with respect to the "y" direction of the scanned area. In Figure 3(c), the crystal orientation map is displayed with respect to the "z" direction of the image plane, which is the direction perpendicular to the scanned area. All crystal orientation maps have been overlapped with the index map to improve data representation. In Figure 3(d), a representative hexagonal prism displays with main colors the three faces of the color map code necessary to interpret the crystal orientation map. Overall, the nanowire revealed a polycrystalline nature, comprising a variety of grain sizes and orientations. Small grains with variable orientations are observed at the tip, and some sparse in other parts of the nanowire; whereas larger grains, mostly oriented towards the [0001] direction, are observed to compose most part of the nanowire. The disorientation among grains ranges from 21° to 70° (supplementary Figures S7 and S8).

DISCUSSION

For isolated nanowires, the orientation of the magnetization results from the competitive interaction between the

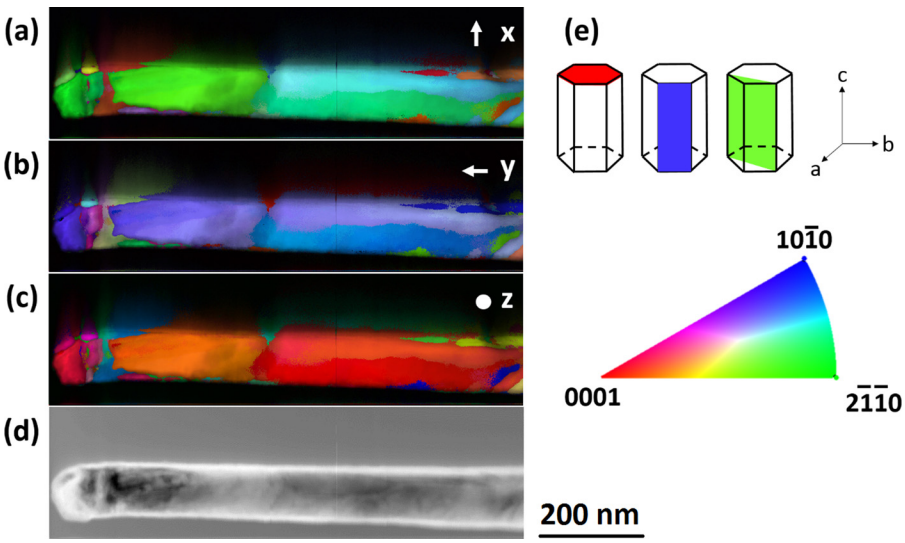

FIG. 3. Crystal orientation map of the Co nanowire with color code with respect to (a) x, (b) y and (c) z. The y direction of the scanned area is aligned roughly along the axis of the nanowire. All crystal orientation maps have been overlapped with the index map. (d) Virtual bright field image of the nanowire. (e) The three facets from the orientation color code map are illustrated in the hexagonal prism.

magnetocrystalline and shape anisotropy. The shape anisotropy energy E_{sh} results from the inner demagnetizing field (proportional to NxM_s, where N the demagnetizing factor and M_s the saturation magnetization) and is given by[39]

$$E_{sh} = \frac{1}{2}\mu_0 N M_s^2, \tag{4}$$

where μ_0 is the magnetic permeability of vacuum ($4\pi \times 10^{-7}$ H/m). For the hard shape direction (i.e., perpendicular to the longitudinal nanowire axis) of an elongated wire with high aspect ratio, N = ½. By using M_s of Co (=1425 kA/m) we have for $E_{sh} = 12.7 \times 10^5$ J/m^3. On the other hand, the magnetocrystalline anisotropy energy, E_{mc}, in terms of the angle θ between the nanowire's main axis and the magnetization vector M, is given by[39]

$$E_{mc} = K_1 \cos^2\theta + K_2 \cos^4\theta, \tag{5}$$

where K_1 and K_2 stand for the first and second magnetocrystalline anisotropy constants. For the hard crystalline direction of the nanowire, $\theta = 0$ (i.e., parallel to the nanowire main axis) and, by considering $K_1 = 4.5 \times 10^5$ J/m^3 and $K_2 = 1.4 \times 10^5$ J/m^3 for Co,[39] we have $E_{mc} = 5.9 \times 10^5$ J/m^3. Therefore, the preferred magnetization orientation is favored energetically with direction parallel to the longitudinal nanowire axis. The similar energy density for both contributions E_{sh}, E_{mc}, is indicative of the competitive interaction between them. Our electron holography results (Figure 2) confirm that shape anisotropy has a predominant role to determine the nanowire's magnetization direction along its main axis, a tendency favored by large elongated grains along the longitudinal axis, with small disorientation from the normal direction, as revealed by the orientation map. In contrast, at the tip of the nanowire, the random distribution of easy axis has a greater influence over the magnetization direction. The nanowire's magnetization and its crystalline phase orientation map are shown in Figure 4. The effect of the crystalline structure on the magnetization is clearly observed at the tip of the nanowire where the random crystal orientation of the grains induced marked fluctuations on the magnetic flux. The wavy nature of the magnetization within larger grains is also influenced by the grain orientation and grain boundaries among crystallites. The Co nanowire is composed of several hcp grains with different orientations. The grain size, as well as the crystal orientation of the grains varies along the nanowire's length, including several large grains (200–300 nm) with the [0001] *c*-axis lying nearly perpendicular to the long axis of the nanowire. The c-axis is the easy axis of the magnetocrystalline anisotropy in hcp Co.[40] The tip of the nanowire containing smaller grains (<80 nm) presents the most disoriented region. In Figure 4(a), the crystal orientation map with respect to z is over-layered with the reliability map. In the reliability map, low reliability values are displayed as dark dots when two or more solutions of the indexation are closer, meaning that crystal grains are superimposed. A similar condition occurs at the grain boundaries since both orientations also contribute to the diffraction pattern.

Figure 4(b) shows the corresponding magnetization map to the crystalline region pictured in Figure 4(a). Even though the observed magnetic flux lines run wavy rather than straight along the length of the nanowire they follow roughly the shape anisotropy, confirming the prevailing influence of the shape anisotropy on the magnetization orientation. The color of the magnetic flux lines indicates the direction of magnetization as represented by the color wheel. Most of the magnetic flux lines point towards the tip of the nanowire shown in the picture, following the long axis direction, but in some areas, the magnetic flux lines show alternating colors, suggesting a change in the direction of magnetization. A vortex structure is present at the tip of the nanowire where the magnetic flux lines follow a clockwise direction. The uncompensated flux lines of this magnetic structure causes stray fields observed as flux leakage. The observed vortex lies along the main axis of the nanowire, as a consequence of the local competing easy axis promoted by the random orientation of the polycrystalline structure at the tip. To the best of our knowledge, this is the first report concerning the use of electron holography and scanning precession-electron diffraction to describe the effect of crystalline orientation on the magnetic structure of high aspect ratio nanowires. Unlike most reports concerning monocrystalline or polycrystalline magnetic nanowires,[30,41,42] in which the formation of domain walls is located along their longitudinal axis (i.e., beyond the tip), for the Co nanowire shown here, no domain wall is observed due to the predominant influence of shape anisotropy along the wire's main axis and to the local

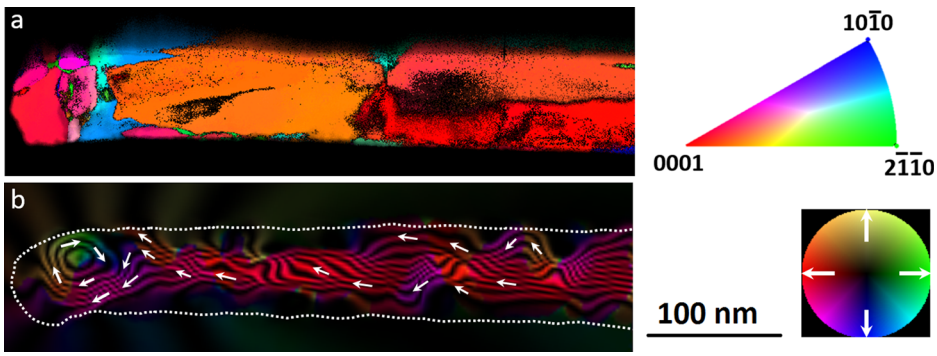

FIG. 4. (a) Crystal orientation and (b) magnetic phase contour maps of the Co nanowire. The crystal orientation map is displayed with respect to the direction of observation z (color key code displayed on the right) and is over-layered with the reliability map to reveal zones where crystallites overlap. The magnetic phase contour map is obtained after amplifying 3 times the cosine of the unwrapped magnetic phase (magnetic flux direction color-wheel displayed on the right). The outline of the nanowire is marked by the thin white line. Arrows represent the magnetic flux direction.

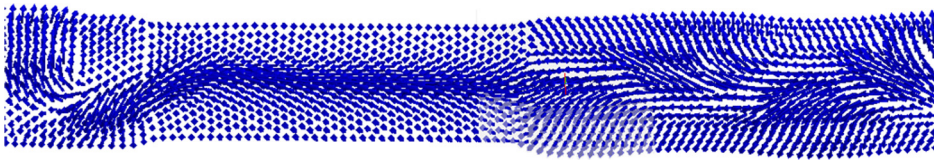

FIG. 5. Calculated magnetization for the micromagnetic Co nanowire model, corresponding to a plane view intersecting the middle part of the model along its longitudinal axis. Grain disorientation information (relative to z axis, Figure 3) was taken from crystalline orientation map of Figures 3 and 4.

competing magnetocrystalline anisotropy axis at the tip. This marked correlation between crystal structure and magnetization distribution is discussed in further detail in the following.

In order to gain further insight for the correlation between magnetic and crystalline structure for the studied Co nanowires, micromagnetic simulations were performed for a cylindrical model with dimensions extracted from TEM images, namely, 95 nm diameter and 1000 nm length. The polycrystalline nature of real nanowire was represented by means of regular segments of different lengths along the wire main axis (short regular grains of 65 nm length at the tip together with large, elongated grain of 200 and 300 nm beyond the tip). For all the grains, different c-axis orientations of the hcp Co structure were assigned according to the orientation map from which the largest disorientations at the tip with smaller grains were taken as representative values for the corresponding smaller grains of our model. The magnetocrystalline anisotropy direction within each grain was set according to *c*-directions. Micromagnetic calculations were carried out by means of the dynamic magnetization description given by the Landau-Lifshitz Gilbert equation of motion and its time integration technique by means of finite element methods,[43] with the following parameters for hcp cobalt: magnetocrystalline constant $K_1 = 4.5 \times 10^5$ J/m^3 and $K_1 = 1.4 \times 10^5$ J/m^3, saturation magnetization $M_s = 1425$ kA/m and exchange constant $A = 3.1 \times 10^{-11}$ J/m.[39]

The calculated magnetization for the Co nanowire model, corresponding to a plane view intersecting the middle part of the model along its longitudinal axis, is shown in Figure 5. In general, the calculated magnetization is consistent with the magnetic contours shown in Figure 4(b), since the magnetization tendency follows the axial direction and, at the tip, a vortex structure is visible, including surrounding magnetization arrows pointing towards the external surface of the model giving rise to flux leaking (not shown in the figure). No domain walls structures are observed beyond the tip along the length of the nanowire, and some wavy magnetization orientations are also visible, both features being in agreement with the electron holography results of Figure 4(b).

Although the experimental magnetic contours reveals the major influence of the shape anisotropy on the nanowire's magnetization, the more detailed magnetic configuration shown in Figure 4(b) suggests that the interfaces between disoriented grains must play a more active role on the magnetization changes of crystals with variable orientations. In particular, the calculated magnetization distribution of the random polycrystalline structure at the tip suggests a counterbalancing effect of the shape anisotropy as a consequence of local competing magnetocrystalline easy axis, which allows vortex formation. The interfaces between strongly disoriented grains can produce surface charges, similar to those characterizing Bloch walls, which in turn produces uncompensated flux lines coming out at the nanowire surface.

On the other hand, the experimental magnetic phase contours of large, elongated grains with c-axis oriented perpendicularly to the longitudinal axis (colored in red and orange in Figure 4(a)), present magnetic wavy flux variations. Such disorientations have been described analytically in equivalent Co nanowires[10] for which the magnetization modulates its orientation along the longitudinal axis, in order to reduce the demagnetizing energy at the equilibrium state. The modulation angle $\theta = \cos(ky)$ leads to a magnetization M function (along the x-y plane, Figure 3), given by[43]

$$M = M_s[\sin(\cos(ky)), \cos((\cos(ky))]. \quad (6)$$

The magnetization configuration given by Eq. (6) is consistent with both, the experimental magnetic contours (Figure 4) and the micromagnetic calculation of the magnetization distribution for large, elongated grains (>300 nm length) with their c-axis oriented perpendicularly to the main nanowire axis. Thus, for large grains with perpendicular c-axis orientation, the predominant effect determining the magnetization orientation comes from the competition between shape and magnetocrystalline anisotropies.

CONCLUSION

In summary, we present a novel combination of advanced electron microscopy techniques, namely, electron holography and precession electron diffraction-assisted crystal phase orientation mapping to visualize the detailed correlation between magnetic and crystal structure of Co nanowires of high aspect ratios. The magnetic structure features were explained in terms of the predominant influence of shape anisotropy at large grains and of the local competing magnetocrystalline anisotropies axis for the small, random oriented grains at the tip. Micromagnetic simulations confirmed the influence of grain disorientation and grain interfaces on the magnetic structure of the studied nanowire, including the asymmetry of the flux leakage and the longitudinal vortex structure observed on the magnetization map. Therefore, this approach is of great value to display specific areas of the material where the magnetocrystalline anisotropy plays a major role over the shape anisotropy. The combination of advanced electron microscopy techniques such as off-axis electron holography and PED-assisted crystal phase orientation mapping has demonstrated fundamental insight on the local magnetic structure of nanoscale materials.

EXPERIMENTAL SECTION

Co nanowires were synthesized inside anodic aluminum oxide (AAO) templates containing columnar nanopores (95 +/− 5 nm diameter) by electrochemical deposition from an aqueous solution of 155 g/l $CoSO_4 \cdot 7H_2O$ and 50 g/l H_3BO_3. The latter was used to maintain the pH of the solution at 5.8. First, one side of each AAO template was coated with Ti(20 nm)/Cu(200 nm). This side was then adhered to a Cu contact and sealed using polyacrylate. The open side of the template was then exposed to the aqueous electrolyte cyclic voltammetry was used to determine the cathode position for Co deposition (−1 V respect to Ag/AgCl reference electrodes).

Electron holography and PED-ACOM were carried out in a JEOL ARM microscope operated at 200 kV. Off-axis electron holography was performed under Lorentz conditions, where the main objective lens is switched off, and the imaging is achieved using the objective minilens (Lorentz lens). For PED-ACOM, the scanning step size was set to 1 nm with a spot size of 1.1 nm in nano-beam diffraction mode using a 20 μm condenser aperture, covering an area of 250 nm × 900 nm. The precession angle was set to 0.9° and the precession unit was operated at 50 Hz. Each pattern was acquired at 0.04 s, and the total acquisition mapping time lasted around 30 min. About 90–100 nm width nanowires were chosen for the study. For the crystal phase orientation analysis, we used off-line data processing software by computing the correlation index between the experimental spot pattern and the calculated spot pattern in the template. Crystallographic data for the Co nanowire is available in the supplementary material.[44]

ACKNOWLEDGMENTS

The authors would like to acknowledge the NSF PREM DMR #0934218 and the Department of Defense #64756-RT-REP. The microscopy work was supported by the National Institute on Minority Health and Health Disparities (NIMHD) in the program Research Centers in Minority Institutions Program (RCMI) Nanotechnology and Human Health Core (G12MD007591). I. Betancourt acknowledges DGAPA, UNAM and CONACYT, Mexico, for their financial support during sabbatical leave. I. Betancourt is also grateful to DGTIC, UNAM for its supercomputing facilities access, as well as to Professor Thomas Schrefl, from St Polten University of Applied Science, Austria, for the use of his micromagnetic code.

[1]V. F. Puentes, K. M. Krishnan, and A. P. Alivisatos, Science **291**, 2115 (2001).
[2]T. M. Whitney, P. C. Searson, J. S. Jiang, and C. L. Chien, Science **261**, 1316 (1993).
[3]T. N. Narayanan, M. M. Shaijumon, L. Ci, P. M. Ajayan, and M. R. Anantharaman, Nano Res. **1**, 465 (2008).
[4]A. Fert and L. Piraux, "Magnetic nanowires," J. Magn. Magn. Mater. **200**, 338 (1999).
[5]Y. P. Ivanov, L. G. Vivas, A. Asenjo, A. Chuvilin, O. Chubykalo-Fesenko, and M. Vazquez, Europhys. Lett. **102**, 17009 (2013).
[6]Z. Liu, P. C. Chang, C. C. Chang, E. Galaktionov, G. Bergman, and J. G. Lu, Adv. Funct. Mater. **18**, 1573 (2008).
[7]K. Ounadjela, R. Ferré, L. Louail, J. M. George, J. L. Maurice, L. Piraux, and S. Dubois, J. Appl. Phys. **81**, 5455 (1997).
[8]X. Han, Q. Liu, J. Wang, S. Li, Y. Ren, R. Liu, and F. Li, J. Phys. D: Appl. Phys. **42**, 095005 (2009).
[9]D. Serantes, V. Vega, W. O. Rosa, V. M. Prida, B. Hernando, M. Pereiro, and D. Baldomir, Phys. Rev. B **86**, 104431 (2012).
[10]G. Bergmann, J. G. Lu, Y. Tao, and R. S. Thompson, Phys. Rev. B **77**, 054415 (2008).
[11]R. K. Dumas, P. K. Greene, D. A. Gilbert, L. Ye, C. Zha, J. Akerman, and K. Liu, Phys. Rev. B **90**, 104410 (2014).
[12]E. C. Estrine, W. P. Robbins, M. M. Maqableh, and B. J. H. Stadler, J. Appl. Phys. **113**, 17A937 (2013).
[13]T. Wang, Y. Wang, Y. Fu, T. Hasegawa, F. S. Li, H. Saito, and S. Ishio, Nanotechnology **20**, 105707 (2009).
[14]K. Krycka, J. Borchers, Y. Ijiri, R. Booth, and S. Majetich, J. Appl. Cryst. **45**, 554 (2012).
[15]M. De Graef and Y. Zhu, *Magnetic Microscopy and Its Applications to Magnetic Materials* (Academic Press, New York, USA, 2000), Vol. 36.
[16]S. McVitie and J. N. Chapman, J. Magn. Magn. Mater. **83**, 97 (1990).
[17]J. N. Chapman, R. PloessI, and D. M. Donnet, Ultramicroscopy **47**, 331 (1992).
[18]A. Masseboeuf, C. Gatel, P. Bayle-Guillemaud, Y. Lamy, and B. Viala, J. Magn. Magn. Mater. **321**, 3080 (2009).
[19]R. E. Dunin-Borkowski, M. R. McCartney, D. J. Smith, and S. S. P. Parkin, Ultramicroscopy **74**, 61 (1998).
[20]C. Beeli, B. Doudin, J.-Ph. Ansermet, and P. Stadelmann, J. Magn. Magn. Mater. **164**, 77 (1996).
[21]R. E. Dunin-Borkowski, T. Kasama, A. Wei, S. L. Tripp, M. J. Hÿtch, E. Snoeck, R. J. Harrison, and A. Putnis, Microsc. Res. Tech. **64**, 390 (2004).
[22]K. Maaz, S. Karim, M. Usman, A. Mumtaz, J. Liu, J. L. Duan, and M. Maqboo, Nanoscale Res. Lett. **5**, 1111 (2010).
[23]M. S. Arshad, S. Šturm, J. Zavašnik, A. P. Espejo, J. Escrig, M. Komelj, P. J. McGuiness, S. Kobe, and K. Ž. Rožman, J. Nanopart. Res. **16**, 2688 (2014).
[24]M. Gallaugher, N. Brodusch, R. Gauvin, and R. R. Chromik, Ultramicroscopy **142**, 40 (2014).
[25]A. Akhtari-Zavareh, L. P. Carignan, A. Yelon, D. Menard, T. Kasama, R. Herring, R. E. Dunin-Borkowski, M. R. McCartney, and K. L. Kavanagh, J. Appl. Phys. **116**, 023902 (2014).
[26]J. Cantu-Valle, E. Díaz Barriga-Castro, V. Vega, J. García, R. Mendoza-Reséndez, C. Luna, V. M. Prida, K. Nielsch, F. Mendoza-Santoyo, M. Jose-Yacaman, and A. Ponce, J. Magn. Magn. Mater. **379**, 294 (2015).
[27]N. Biziere, C. Gatel, R. Lassalle-Balier, M. C. Clochard, J. E. Wegrowe, and E. Snoeck, Nano Lett. **13**, 2053 (2013).
[28]T. P. Almeida, T. Kasama, A. R. Muxworthy, W. Williams, L. Nagy, T. W. Hansen, P. D. Brown, and R. E. Dunin-Borkowski, Nat. Commun. **5**, 5154 (2014).
[29]C. Phatak, Y. Liu, E. B. Gulsoy, D. Schmidt, E. Franke-Schubert, and A. Petford-Long, Nano Lett. **14**, 759 (2014).
[30]K. Gandha, K. Elkins, N. Poudyal, X. Liu, and J. P. Liu, Sci. Rep. **4**, 5345 (2014).
[31]M. Körner, F. Röder, K. Lenz, M. Fritzsche, J. Lindner, H. Lichte, and J. Fassbender, Small **10**, 5161 (2014).
[32]S. Estradé, J. Portillo, J. Mendoza, I. Kosta, M. Serret, C. Müller, and F. Peiró, Micron **43**, 910 (2012).
[33]T. L. Daulton, K. S. Bondi, and K. F. Kelton, Ultramicroscopy **110**, 1279 (2010).
[34]E. F. Rauch and M. Véron, Mater. Charact. **98**, 1 (2014).
[35]A. Avilov, K. Kuligin, S. Nicolopoulos, M. Nickolskiy, K. Boulahya, J. Portillo, G. Lepeshov, B. Sobolev, J. P. Collette, N. Martin, A. C. Robins, and P. Fischione, Ultramicroscopy **107**, 431 (2007).
[36]J. Cantu-Valle, F. Ruiz-Zepeda, F. Mendoza-Santoyo, M. José-Yacaman, and A. Ponce, Ultramicroscopy **147**, 44 (2014).
[37]F. Ruiz-Zepeda, Y. L. Casallas-Moreno, J. Cantu-Valle, D. Alducin, U. Santiago, M. José-Yacaman, M. López-López, and A. Ponce, Microsc. Res. Tech. **77**, 980 (2014).
[38]E. Völkl, L. F. Allard, and D. C. Joy, *Introduction to Electron Holography* (Springer, New York, USA, 1999).
[39]H. Kronmuller and M. Fahnle, *Micromagnetism and the Microstructure of Ferromagnetic Solids* (Cambridge University Press, Cambridge, UK, 2003).
[40]J. M. D. Coey, *Magnetism and Magnetic Materials* (Cambridge University Press, Cambridge, UK, 2009).
[41]Y. P. Ivanov, D. G. Trabada, A. Chuvilin, J. Kosel, O. Chubykalo-Fesenko, and M. Vazquez, Nanotechnology **25**, 475702 (2014).

[42]Y. P. Ivanov, M. Vazquez, and O. Chubykalo-Fesenko, J. Phys. D: Appl. Phys. **46**, 485001 (2013).
[43]T. Schrefl, G. Hrkac, S. Bance, D. Suess, O. Ertl, and J. Fidler, in *Handbook of Magnetism and Advanced Magnetic Materials*, edited by H. Kronmuller and S. Parkin (John Wiley & Sons, New York, USA, 2007), Vol. 2.
[44]See supplementary material at http://dx.doi.org/10.1063/1.4923745 for details of the reconstruction phase of the holograms and crystal phase analysis.